ENHANCED DENSIFICATION OF METAL POWDERS BY TRANSFORMATION-MISMATCH PLASTICITY

C. SCHUH[1], P. NOËL[2] and D. C. DUNAND[1]†

[1]Northwestern University, Department of Materials Science and Engineering, 2225 N. Campus Drive, Evanston, IL 60208-3108, USA and [2]Matra Défense, BP 150, 78141, Vélizy, France

Abstract—The densification of titanium powders is investigated in uniaxial die pressing experiments carried out isothermally at 980°C (in the β-field of titanium) and during thermal cycling between 860 and 980°C (about the α/β phase transformation of titanium). Thermal cycling is found to enhance densification kinetics through the emergence of transformation-mismatch plasticity (the mechanism responsible for transformation superplasticity) as a densification mechanism. The isothermal hot-pressing data compare favorably with existing models of powder densification, and these models are successfully adapted to the case of transformation-mismatch plasticity during thermal cycling. Similar conclusions are reached for the densification of titanium powders containing 1, 5, or 10 vol.% ZrO_2 particles. However, the addition of ZrO_2 hinders densification by dissolving in the titanium matrix during the hot-pressing procedure. © *2000 Acta Metallurgica Inc. Published by Elsevier Science Ltd. All rights reserved.*

1. INTRODUCTION

High-temperature compaction of powders is a well-established technique to produce metal, ceramic or metal–ceramic composite items with negligible porosity. As compared to pressureless sintering, compaction is accelerated by the application of stresses that are either isostatic, e.g., in Hot-Isostatic-Pressing (HIP), or combined deviatoric and isostatic, e.g., in uniaxial die hot-pressing. Time, pressure and temperature are the three main process parameters which must be minimized to increase productivity (governing parameter: time), reduce equipment costs (governing parameters: temperature and pressure) and minimize microstructure degradation such as second-phase coarsening, grain growth or matrix-reinforcement reaction in composites (governing parameters: time and temperature). Continuum or micromechanical approaches have been used to model the densification kinetics of metal powders as a function of these process parameters and powder materials properties [1–8]. Typically, densification is modeled in two stages: the initial stage, for relative densities below about 90%, where the powder particles retain their identity, and the final stage, for relative densities above about 90%, where pores are isolated within a dense

matrix. Modeling of the initial stage combines mechanical considerations (deformation of pairs of contacting spheres) with geometric considerations (coordination number of individual spheres), while modeling of the second stage considers the shrinkage of pores within a continuum matrix. There have also been several studies on the densification of blends of ceramic and metal powders for composite fabrication (e.g., Refs [9–16]). Experimental results on such systems are similar to those for densification of unreinforced metals [9, 10], but exhibit lower densification rates due to stress partitioning effects.

The initial stage of metal powder densification is characterized by plastic deformation of the powders in contact with each other at neck areas. Deformation, and thus preform compaction, can occur by surface diffusion, or by any of the deformation mechanisms active for deformation of bulk metals, i.e. time-independent plastic yield and time-dependent deformation by diffusional or dislocation creep. Any other deformation mechanism operational in bulk metals or composites can thus in principle be utilized for powder densification. One such mechanism is internal-stress plasticity, resulting from the biasing of internal mismatch strains by an external stress. In unreinforced bulk materials, internal mismatch stresses are produced between grains with anisotropic coefficient of thermal expan-

---

† To whom all correspondence should be addressed.

sion during a thermal excursion (e.g., Zn and U [17]) or between grains undergoing an allotropic phase transformation during crossing of the transus temperature (e.g., Ti, Zr, Co, Fe and U [18]). In bulk composites, mismatch stresses result between matrix and reinforcements exhibiting different thermal expansion upon thermal cycling (e.g., Al–SiC [19–21]) or different compressibility upon pressure cycling (e.g., Pb–Al_2O_3 [22]). Alternatively, mismatch stresses can be produced when one of the phases (e.g., the matrix) undergoes a phase transformation while the other (e.g., the reinforcement) does not, as reported in the Ti–TiC system [23–25]. In all the above cases, when the material is deformed under a uniaxial stress while the temperature is repeatedly cycled, the flow stress is reduced as compared to isothermal deformation, the average strain rate is linear in stress and very large elongations to fracture can be attained, leading to mismatch-induced superplasticity. The increased strain rates observed in bulk materials deforming under these conditions is particularly interesting for powder densification, since it could accelerate densification kinetics. To the best of our knowledge, only two of the above mismatch-plasticity mechanisms have been used in powder densification, i.e. transformation-mismatch superplasticity in metallic powders [26–30] and compressibility mismatch superplasticity in metal–ceramic powder blends [22, 31], as described in more detail in the following.

Kohara [26], Oshida [27], and Ruano et al. [28] applied the concept of transformation-mismatch superplasticity to the compaction of ferrous powders. Under a small compressive stress (about 0.04 MPa and 1–3 MPa, respectively), Kohara [26] and Oshida [27] demonstrated enhanced densification of pure iron during cycling through the α/γ phase transformation. In similar cycling experiments on white cast iron, Ruano et al. [28] identified the useful uniaxial pressure range as 3–35 MPa. They also concluded that, because of the low temperature and short times associated with cyclic transformation hot-pressing, the fine structure of rapidly-solidified powders could be retained, unlike conventional isothermal compaction for which higher temperatures lead to coarsening of the microstructure. Subsequently, Leriche et al., [29, 30] investigated hot-pressing of Ti-6Al-4V powders under a relatively high stress of 30 MPa at constant temperatures (800, 920 and 1040°C) or under temperature cycling conditions (800–1040°C). Both the cycling and the isothermal experiment in the β-range (1040°C) lead to densities above 99%, while the isothermal densification at lower temperatures gave significantly lower densities. The authors calculated the contribution to densification from transformation superplasticity during the first and second cycles and concluded that it was larger than the contribution of creep. Schaefer and Janowski [32] observed enhanced densification during HIP of a

TiAl alloy due to a single, irreversible transformation from metastable α_2 to stable γ phase. Recently, Huang and Daehn [22, 31] demonstrated that compressibility mismatch superplasticity could be used to densify powder blends. They subjected pure lead powders with 0, 10, 20 and 40 vol.% alumina particles to up to 100,000 stress cycles between 0 and up to 500 MPa at frequencies between 1 and 10 Hz at room temperature. As expected, if internal-stress superplasticity is the controlling densification mechanism, the densification rate was higher under stress cycling conditions than under static conditions. This enhancement increased with volume fraction of alumina and for higher maximum stresses, but it was insensitive to frequency. The authors calculated that the mismatch stresses were high enough to induce plasticity in the dense composites, but did not extend their analysis to the state of stress during powder compaction.

In the present article, we demonstrate that densification of pure titanium powders and titanium–zirconia powder blends is enhanced during thermal cycling through the allotropic phase transformation of titanium. Special attention is given to the effect of thermal cycling on the range of dominance of densification mechanisms for initial stage densification (i.e., relative density below about 90%) as well as final stage densification (relative density above 90%). The purpose of this work is two-fold. First, we confirm for pure titanium the enhancement of densification rate obtained by thermal cycling about the α/β transformation range, as reported for cast iron [28] and Ti-6Al-4V powders [29, 30]. These experiments provide a basis for theoretical analysis of transformation-mismatch plasticity as a densification mechanism. Secondly, we demonstrate that this effect is also present during compaction of composite powders, potentially providing a means for rapid production of discontinuously-reinforced composites.

2. EXPERIMENTAL PROCEDURES

The titanium powders used in all of the experiments (from Cerac, Milwaukee, WI) were equiaxed but irregular in shape and had a size between 80 and 106 μm. They contained 0.49 wt% O, 0.04 wt% Fe, 0.002 wt% Zr, 0.001 wt% N. The approximate α- and β-transus temperatures corresponding to this oxygen content are 910°C and 950°C, respectively [33]. The partially-stabilized zirconia powders (Amperite 825-1 from Starck, Germany) were also irregular in shape and had a size between 25 and 45 μm. Their composition was 7 wt% Y_2O_3, 0.4 wt% SrO_2, 0.3 wt% TiO_2, 0.2 wt% Al_2O_3, balance ZrO_2. Zirconia was chosen because of its high coefficient of thermal expansion, $\alpha(\alpha_{ZrO_2} = 10.5 \cdot 10^{-6}/K$ between 800°C and 1000°C [34]), minimizing thermal mismatch with titanium ($\alpha_{\beta-Ti} = 10.8 \cdot 10^{-6}/K$ between 900°C and 1100°C

[35]) and thus the contribution of thermal-mismatch plasticity.

Figure 1 shows a schematic view of the hot-pressing apparatus, which is similar to, but larger than, that described in Ref. [10]. A total mass of 18 g of titanium powders mixed with 0, 1, 5, or 10 vol.% zirconia powders (reinforcement volume fractions are referred to dense Ti–ZrO$_2$ composites) was placed in a cylindrical TZM molybdenum die. The die had an inside diameter of 36.4 mm and was lined with stainless steel foil. A TZM molybdenum piston transmitted the uniaxial force to the powders, which were contained at the other end of the cylinder by a TZM molybdenum base. Both piston and base were separated from the powder by two 50 μm thick titanium and steel foils, and all metallic parts were coated with boron nitride to prevent reaction and to provide lubrication. The assembly was sandwiched between two graphite susceptors producing and conducting heat generated by a water-cooled induction coil. A constant load was transmitted to the assembly by two quartz columns and by a cross-head outfitted with an O-ring, insuring a low-friction, leak-free motion between the head and the quartz tube separating the evacuated assembly from the atmosphere. The powder temperature was monitored by a K-type thermocouple in contact with the molybdenum piston.

Prior to heating, the powders were compacted in the apparatus at room temperature under a pressure of 90.5 MPa. Heating to the test temperature took place under a small applied stress of 0.16 MPa at a rate of 5 K/s and with degassing periods of at most 30 min at 300, 600 and 920°C. In isothermal experiments, the temperature was raised to 980°C (in the β-field of Ti) and maintained constant throughout the experiment. In cycling experiments, the temperature was varied between 860°C and 980°C over cycles of 143 s duration, with heating and cooling ramps of 55 s and 88 s, respectively. Throughout the experiments, a stepping motor kept the applied pressure on the preform constant at a level of 1.04 MPa or 2.92 MPa (rounded in what follows as 1 MPa and 3 MPa, respectively), while a vacuum of $4 \cdot 10^{-4}$ mbar was maintained by a turbomolecular pump. Powder compaction was monitored by measuring the displacement of the cross-head with a laser extensometer accurate to ± 2 μm. To eliminate errors resulting from the load train and specimen thermal expansion and contraction during the cycling experiments, the displacements were measured at the same temperature for each cycle, i.e., at the lowest temperature of the cycle.

The time-dependence of the compact density was determined from the final density of the compact and the position of the cross-head during the experiment, assuming conservation of mass. Metallographic preparation consisted of polishing with diamond pastes of size 30 μm, 9 μm and 3μm, as well as submicron colloidal silica.

3. RESULTS

3.1. Precompaction experiments

Because the initial density of the preform is an important parameter, preliminary experiments were conducted by subjecting the powders to the cold compaction step at 90.5 MPa, heating under a pressure of 0.16 MPa to a maximum temperature between 790 and 930°C, and cooling immediately thereafter without applying the test pressure of 1 MPa or 3 MPa. Table 1 lists the compact relative densities (referred to simply as density in the rest of this article) which are constant at $\rho_o = 0.64 \pm 0.03$, close to the density for randomly packed spheres, ~0.62. Assuming that little densification took place during the rapid excursion at high temperature under negligible applied stresses, these results indicate that the presence of up to 10 vol.% ZrO$_2$ par-
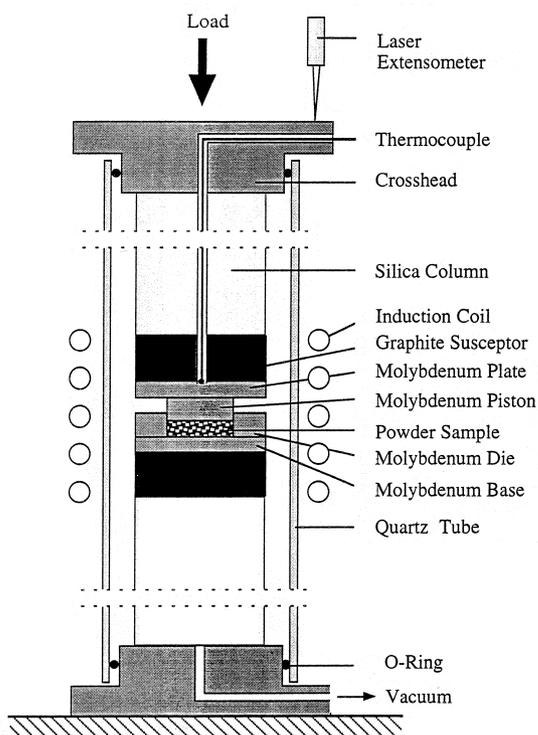

Fig. 1. Schematic drawing of hot-pressing apparatus.

Table 1. Relative densities of samples subjected to cold compaction with applied stress 90.5 MPa, heating to a maximum temperature under a small applied stress of 0.16 MPa, and cooling without substantial densification

ZrO$_2$ content (vol.%)	Maximum temperature (°C)	Relative density
0	930	0.66
1	870	0.62
5	790	0.61
10	910	0.64

ticles does not affect the density of the compacts, in agreement with results by Lange *et al.* [36] on cold pressing of aluminum or lead powders containing steel inclusions.

Figure 2 shows the structure of the pure Ti compact just before the application of the test load, i.e., after cold compaction and a temperature excursion to 930°C under the low stress of 0.16 MPa. While the individual powder particles are non-spherical, the shape of powder protuberances is rounded, so that local contacts between particles can be expected to be similar to contact between spherical powders.

3.2. Isothermal and thermal cycling densification

The relative density, ρ, of the various powder blends subjected to isothermal compaction (980°C) or thermal cycling compaction (860–980°C) are shown as a function of time in Fig. 3 for applied stresses of 1 and 3 MPa. The measured rates of densification generally increase with applied stress and decrease with volume fraction of non-densifying ZrO_2 addition.

The rate of densification during thermal cycling through the α/β phase transformation of Ti is increased relative to isothermal compaction for most of the compositions at either 1 MPa or 3 MPa. For example, the unreinforced titanium powder compacted by thermal cycling at 3 MPa reached full theoretical density after about 125 min, compared with approximately 250 min for isothermal densification. The only exception to this trend is the 10% ZrO_2 composition compacted at 1 MPa, which densified more slowly than the specimen compacted isothermally at the same stress.

4. DISCUSSION

In the following sections, we consider the experimental results in light of the successful densification models of Arzt, Ashby, and coworkers [1, 3, 4, 37, 38], who model densification on a mechanistic basis, assuming that the behavior of the compact can be adequately described by a local configuration of average, mono-sized spherical particles (in the initial stage of densification) or of voids (in the final stage). We first consider the initial stage of densification, where powder particles maintain their identity but gradually increase their coordination as densification proceeds. This geometry has typically been considered valid for densities below about 0.90, above which pores become isolated. After this point, models for the shrinkage of isolated spherical voids are used to predict densification rates. We thus treat this final stage of densification separately in a following section.

We apply these models for spherical powders, despite the irregular shape of both the titanium and ZrO_2 powders. This approach is justified by experiments [5] showing that both angular and spherical titanium powders exhibit similar densification behavior at 700°C at preform densities above 0.70, despite initial packing densities much lower for the former (0.42–0.54) than the latter (about 0.64) powders. This was explained by the rapid deformation of angular powders in the very early stage of densification, until they reached densities similar to those of spherical powders. The curved interparticle contacts observed in Fig. 2 and the high pre-densification packing density ($\sim$0.64) of our powders further justify this approach.

In what follows, we first consider the case of unreinforced titanium, for which these models can
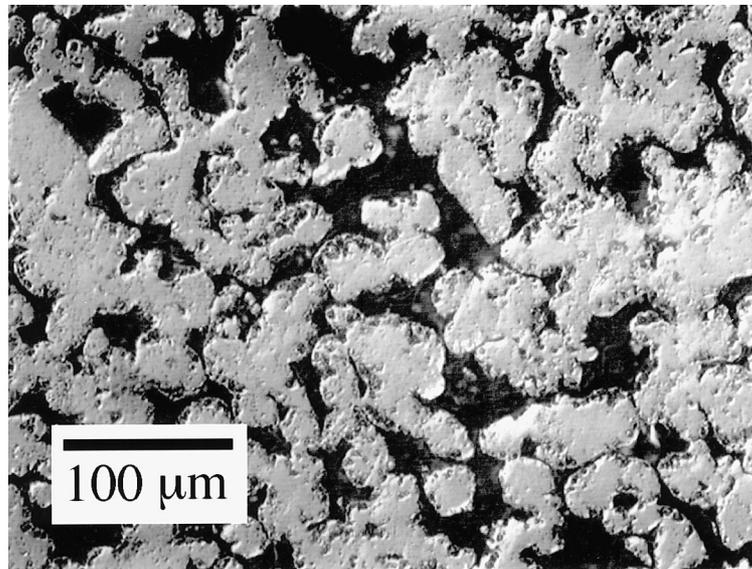

Fig. 2. Metallographic section of Ti powders after the cold-pressing procedure described in the text, and before hot densification.

be applied without substantial modification. The constitutive equation of transformation-mismatch plasticity is incorporated into the analytical models to predict the contribution of this new deformation mechanism to densification. We then discuss the densification of the ZrO_2-containing composite powder blends relative to that of the unreinforced titanium powders.

4.1. Initial stage densification of unreinforced titanium powders

4.1.1. Isothermal densification theory. The initial-stage densification models developed by Arzt, Ashby, and coworkers [1, 3, 4, 37, 38] consider the geometry of densification and particle coordination, as well as the kinetics of several densification mechanisms. These include time-independent yielding, power-law creep, and diffusion of matter to inter-particle boundaries, either through the bulk or at the interparticle interfaces. Although these authors have considered diffusional creep processes for ma-

terials with a small grain size relative to the powder particle size, the rapid grain growth of titanium in the β-phase insures a grain size on the order of the particle size, making the contribution of diffusional creep negligible. The three remaining mechanisms of diffusion, dislocation creep, and yield are summarized in the work of Helle *et al.* [4], who provide simplified rate equations describing densification by each mechanism. These approximate solutions are presented in turn in the following paragraphs, with the following recurring symbols: $\dot{\rho}$ is the time-derivative of the compact density (i.e., densification rate), $\rho_o = 0.62$ is the density of a randomly-packed spherical powder prior to the start of densification, r is the radius of the average powder particle, and the effective interparticle contact pressure P_{eff} is given by:

$$P_{eff} = B_i \cdot \frac{(1 - \rho_o)}{\rho^2 \cdot (\rho - \rho_o)} \cdot P \qquad (1)$$

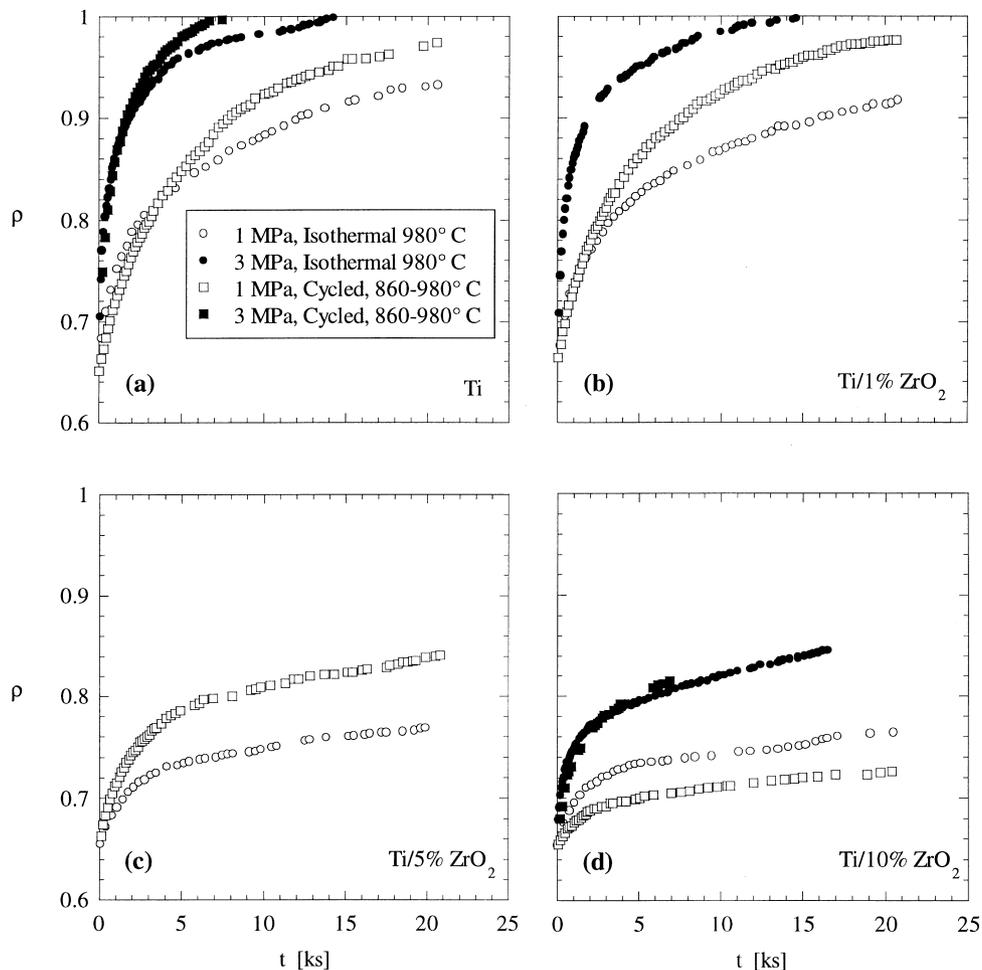where P is the externally-applied pressure and B_i is

Fig. 3. Relative density as a function of compaction time for titanium powders containing (a) 0 vol.% ZrO_2, (a) 1 vol.% ZrO_2, (c) 5 vol.% ZrO_2, and (d) 10 vol.% ZrO_2.

a constant introduced by Taylor *et al.* [10], which depends on the compaction geometry and is discussed in more detail later.

Diffusional densification occurs by two diffusion paths (i.e., through the powder particle volume or along the interparticle boundary) which transport matter from the interior of powder particles to the interparticle contacts, increasing the area of such contacts. Helle *et al.* [4] have combined the effects of these two diffusion paths into a single simplified rate equation:

$$\dot{\rho} = 43 \cdot \frac{\Omega}{k \cdot T \cdot r^3} \cdot \frac{\rho^2 \cdot (1 - \rho_o)}{(\rho - \rho_o)} \cdot (\delta D_b + r \cdot (\rho - \rho_o) \cdot D_v) \cdot P_{eff} \quad (2)$$

in which Ω is the atomic volume, k is the Boltzmann constant, T is the absolute temperature, δD_b is the boundary diffusion coefficient, and D_v is the volume diffusion coefficient.

Dislocation creep is typically described by a power-law constitutive equation relating the strain rate $\dot{\varepsilon}$ to the applied stress σ [39]:

$$\dot{\varepsilon} = C \cdot \sigma^n \quad (3)$$

where C is a constant incorporating an Arrhenius temperature dependence, and n is the creep stress exponent. By considering creep deformation at interparticle contacts according to equation (3), Helle *et al.* [4] give the following expression for the densification rate:

$$\dot{\rho} = 3.06 \cdot (\rho^2 \cdot \rho_o)^{1/3} \cdot \left(\frac{\rho - \rho_o}{1 - \rho_o}\right)^{1/2} \cdot C \cdot \left(\frac{P_{eff}}{3}\right)^n \quad (4)$$

The case of time-independent yield is handled by the above authors by assuming an infinite densification rate when interparticle contact stresses exceed the yield criterion. As yielding occurs, the interparticle contact area increases to sustain the applied stress, and at a critical density, yielding ceases. The application of this approach to the densification of β–Ti is difficult, as the transition from dislocation creep to time-independent yielding is not well-defined; a regime of increasing stress sensitivity (power-law breakdown) is observed as stress is increased. Frost and Ashby [39] identify the transition from power-law creep to power-law breakdown of β–Ti at a principal stress of approximately $\sigma_t \approx 6.0 \cdot 10^{-3} \cdot G$, where G is the temperature-dependent shear modulus of β–Ti given in Ref. [39]. We take this stress as a fair estimate for the transition from power-law creep to rapid, yield-like deformation of β-Ti. The criterion for yielding during powder compaction as derived from the solution of the plastic indentation problem is [3, 4]:

$$P_{eff} \geq 3 \cdot \sigma_t \quad (5)$$

4.1.2. Thermal cycling densification. During thermal cycling through a phase transformation, the above densification mechanisms remain active. The yield contribution can be evaluated by taking σ_t to be the yield stress of the weakest phase, which for titanium is the β-phase. Diffusional densification and power-law creep densification occur at varying rates during each thermal cycle due to the temperature fluctuation, but can be adequately described by the use of their respective isothermal densification laws [equations (2) and (4)] and an effective temperature during the cycling. The effective temperature is found by integration of the diffusivity over the thermal cycles, as done in, e.g., Ref. [24]. For the present thermal cycles, the effective temperature is found to be ~910°C. This temperature is used to evaluate the contributions of power-law creep and diffusional densification during thermal cycling.

As reviewed earlier, transformation-mismatch plasticity is a deformation mechanism which is observed during thermal cycling through an allotropic phase transformation under the action of external stresses. For small applied stresses, this results in a linear relationship between the applied stress and the effective strain rate, given by Greenwood and Johnson as [18]:

$$\bar{\dot{\varepsilon}} = \frac{4}{3} \cdot \frac{5 \cdot n'}{4 \cdot n' + 1} \cdot \frac{\Delta V}{V} \cdot \frac{1}{\Delta t} \cdot \frac{\sigma}{\sigma_o} \quad (6)$$

where $\bar{\dot{\varepsilon}}$ is the average strain rate during thermal cycling, $\Delta V/V$ is the volume mismatch between the allotropic phases, and Δt is the period of the thermal cycles. The average internal stress generated during the phase transformation, σ_o, is accommodated by a creep process in the weaker phase with a power-law exponent n'. Following the procedure which Arzt, Ashby, and coworkers [1, 3] applied to power-law densification, this constitutive equation can be generalized to three dimensions and applied to densification by analogy to equation (4), yielding the following rate equation:

$$\dot{\rho} = 1.36 \cdot (\rho^2 \cdot \rho_o)^{1/3} \cdot \left(\frac{\rho - \rho_o}{1 - \rho_o}\right)^{1/2} \cdot \frac{5 \cdot n'}{4 \cdot n' + 1} \cdot \frac{\Delta V}{V} \cdot \frac{1}{\Delta t} \cdot \frac{P_{eff}}{\sigma_o} \quad (7)$$

As already noted, transformation-mismatch plasticity is only expected to follow the linear constitutive law of equation (6) for small applied stresses. As the applied stress becomes large compared to the internal transformation mismatch stress, observed deformation rates are more rapid than those predicted by equation (6) [18, 40]. At large applied stresses, the average strain rate $\bar{\dot{\varepsilon}}$ approaches the rates predicted by the power-law of the creeping weaker phase. Therefore, when the interparticle contact pressure is low, equation (7)

for linear transformation-mismatch plasticity is expected to describe densification, while at larger pressures the power-law mechanism dominates [equation (4)]. The range of dominance of these two mechanisms is determined explicitly in the following section.

4.1.3. Densification mechanism maps. The densification equations presented in the previous sections form the basis from which densification mechanism maps can be constructed, as outlined in Ref. [4]. In this section we construct such maps on axes of ρ vs P/σ_t corresponding to the two cases of interest, namely isothermal densification at 980°C (in the β-phase of titanium) and densification during thermal cycling through the α/β phase transformation of titanium. The range of dominance of each mechanism is defined by the conditions of stress and density for which it produces the most rapid densification rate of the several mechanisms. In cases where the yielding criterion [equation (5)] is met, this mechanism is taken as dominant. The initial density, $\rho_o = 0.62$ is the value for randomly-packed spheres [4], and the average particle radius is taken as $r = 45$ μm. The materials properties required to model isothermal densification of β–Ti are provided by Frost and Ashby [39]. These parameters were all accurately measured, with the exception of the diffusivity in the interparticle boundaries, δD_b. We take for this parameter the grain boundary diffusivity of β–Ti, as approximated by Frost and Ashby [39].

Construction of a densification mechanism map during thermal cycling requires much the same information as for the isothermal case. In addition, the transformation volume change is $\Delta V/V = 0.0048$ [24], the stress exponent of the accommodating matrix phase (β–Ti) is $n' = 4.3$ [39], and the cycle duration is $\Delta t = 143$ s. The contributions of the power-law and diffusion densification mechanisms are calculated at the effective cycling temperature of 910°C as described earlier. We note that the calculated maps are relatively insensitive to selection of this temperature within the physically reasonable range 900–950°C.

The final parameter we require to use the transformation-mismatch plasticity densification model [equation (7)] is the average internal stress generated during the phase transformation, σ_o. There are many studies of transformation-mismatch plasticity of titanium in the literature, as summarized in Refs [24, 25]. Of these investigations, Refs [25, 41, 42] have been identified as the most accurate and consistent [25]. By fitting equation (6) to tensile transformation superplasticity data from these studies, the internal stress parameter is found to be $\sigma_o = 3.3$ MPa, the value used here in constructing the densification map. Although this value may be sensitive to the heating rate [43], the thermal cycles used in

the present work are of similar amplitude and duration to those used in Refs [25, 41, 42].

The models of Arzt, Ashby, and coworkers, described and adapted to transformation-mismatch plasticity in the previous sections, assume that densification occurs under isostatic pressure. Therefore, an additional parameter, B_i, must be introduced to adapt these models to the case of constrained uniaxial pressing, as done by Taylor *et al.* [10], for example. This dimensionless constant relates the applied stress state to conditions of pure hydrostatic pressure, and is therefore equal to unity during isostatic pressing. The combined deviatoric and hydrostatic stresses established during uniaxial die pressing have been studied by several authors (e.g., Refs [12, 44, 45]), and it has been noted that a deviatoric stress superimposed upon a hydrostatic stress enhances the rate of densification [45]. Besson and Evans [12] derived a rate equation for power-law densification which applies explicitly to the case of uniaxial pressing. As discussed in Appendix A, by relating this rate equation to the Arzt, Ashby *et al.* power-law densification model [equation (4)],
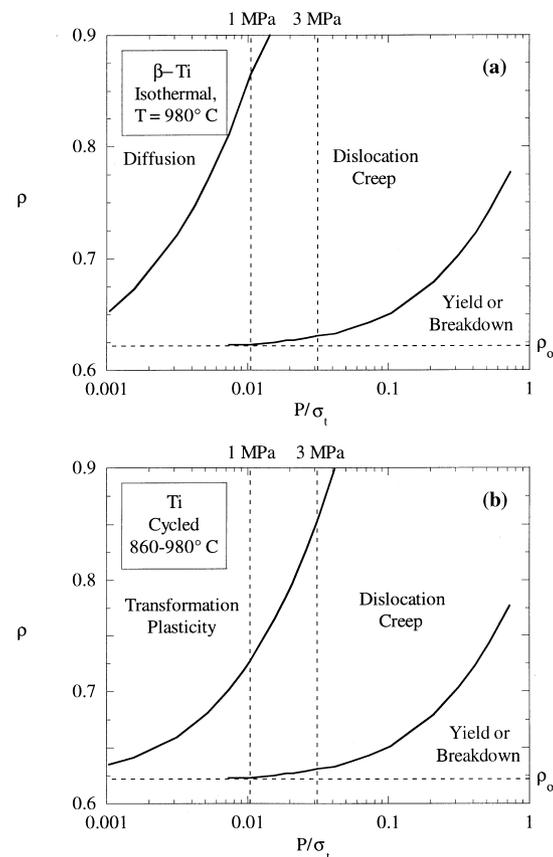

Fig. 4. Densification mechanism maps for unreinforced titanium for conditions of (a) isothermal densification at 980°C, and (b) thermal cycling densification about the α/β phase transformation, with an effective temperature of 910°C. Dashed lines show the experimentally-applied stresses and the initial density ρ_o.

and comparing the result with experimental data from the work of Besson and Evans [12], the constant B_i is found to be about 1.1 for initial stage densification. The value near unity indicates that uniaxial die pressing and isostatic pressing should produce similar densification rates.

The densification mechanism maps for initial-stage isothermal densification of β–Ti at 980°C and thermal-cycling densification between 860 and 980°C are shown in Figs 4(a) and (b), respectively. The general shape of both maps is similar, with yield or power-law breakdown dominant at large pressures and low densities, and power-law creep densification controlling at intermediate pressures and densities. The extent of the yield mechanism is similar for the isothermal and thermal cycling conditions, but the creep field is smaller during thermal cycling than during isothermal densification. In the isothermal case, at low pressures and high densities, power-law creep becomes slow and diffusional densification inhabits a small regime of dominance.

The principal effect of thermal cycling on the densification mechanism map is the disappearance of the diffusional mechanism altogether, in favor of the transformation-mismatch plasticity mechanism, which also dominates densification at relatively low pressures and high densities. Additionally, the emergence of transformation-mismatch plasticity results in notable shrinkage of the dislocation creep field. These observations are technologically significant, as they indicate that thermal cycling will improve densification rates at relatively low applied stresses and/or at small levels of porosity.

4.1.4. Analysis of experimental data. The densification maps in Fig. 4 provide guidance for analysis of the experimental densification data of Fig. 3. The applied stresses used in the experiments (1 and 3 MPa) are shown as dotted vertical lines in Fig. 4. From the positions of these lines, we anticipate that only one of the four experiments performed on unreinforced titanium can be fully described by a single model (isothermal densification at 3 MPa); all of the other data should reflect, to some degree, the operation of two mechanisms. However, if data is selected from appropriate density ranges dominated by a single mechanism, then the theories outlined above can be directly compared to the experimental data.

For comparison with the models, it is convenient to determine the densification rate during the experiments. Given the close spacing of the experimental data in both time and density, it is reasonable to calculate differences between successive points to determine rates. We use this method in what follows, and assume an error in the experimental densification rates of $\pm 50\%$.

Because of the narrow range of applicability of the diffusional densification mechanism with respect to the experimental data [Fig. 4(a)], we limit our atten-

tion to the dislocation creep and transformation-mismatch plasticity mechanisms. According to equations (4) and (7), both of these mechanisms are expected to yield a characteristic relationship between the interparticle contact pressure, P_{eff}, and the quantity $\dot{\rho} \cdot \rho^{-2/3} \cdot (\rho - \rho_o)^{-1/2}$. When these variables are plotted against one another in double-logarithmic fashion, the deformation stress exponent n is given by the slope. For power-law creep of β–Ti a slope of $n = 4.3$ is thus expected, while $n = 1$ should characterize transformation-mismatch plasticity.

Based on the densification mechanism map [Fig. 4(a)], we anticipate that the isothermal densification data will be controlled by the power-law creep mechanism at densities below about 0.86 for
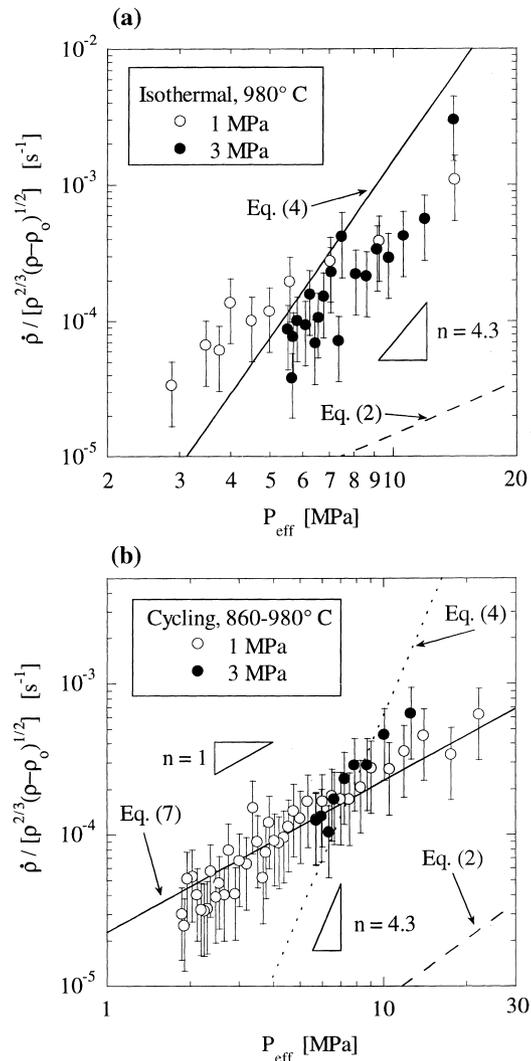

Fig. 5. Double-logarithmic plots of $\dot{\rho} \cdot \rho^{-2/3} \cdot (\rho - \rho_o)^{-1/2}$ vs P_{eff} [equations (4) and (7)] for unreinforced titanium during (a) isothermal densification at 980°C, and (b) thermal cycling densification, 860–980°C, where equations (2) and (4) are calculated at the effective temperature of 910°C. Experimental data are shown as points, and model predictions as solid and dashed lines.

applied pressure of 1 MPa. The data collected with applied pressure of 3 MPa should be dominated by power-law densification over the full range of initial stage densities (0.62–0.9). Experimental data from these stress ranges are shown in Fig. 5(a), with axes as described in the previous paragraph. The two sets of isothermal data fall close together, and are best-fitted with slopes of $n = 2.1$ and 3.3, at $P = 1$ and 3 MPa, respectively. Also shown in Fig. 5(a) are the predictions of equations (2) and (4) using the materials parameters from Ref. [39]. Both the slope and the absolute magnitudes of the experimental data are predicted reasonably well by the power-law creep densification law [equation (4)], while the diffusional densification equation [equation (2)] significantly under-predicts the experimental data. These observations indicate that power-law creep is the dominant densification mechanism, as expected from the densification map [Fig. 4(a)]. Given the many approximations in the use of materials parameters, the limited amount of appropriate experimental data, and the approximate form of the model, the predictions are surprisingly good. Furthermore, although the best-fit curves give values of n below the expected 4.3 for power-law creep, each data set can be described by a line with slope $n = 4.3$ within experimental errors, except for a few outliers.

A similar analysis can be performed for the thermal-cycling experiments, which are expected to be dominated by transformation-mismatch plasticity at densities above 0.75 and 0.87 for applied pressures of 1 MPa and 3 MPa, respectively [Fig. 4(b)]. All of the data are plotted in Fig. 5(b) in the double-logarithmic fashion described above. The two sets of data are nearly coincident, and the data collected at $P = 1$ MPa clearly describe a line with a slope near to unity. According to equation (7), this is the expected trend for densification controlled by transformation-mismatch plasticity. For comparison with the data, the predictions of equation (7) are also shown in Fib. 5(b). The agreement between the data and the model is excellent, particularly since no adjustable parameters were used. However, the transition from transformation-mismatch plasticity [equation (7)] to power-law creep [equation (4)] expected at $P_{\mathrm{eff}} \approx 7$ MPa is not clearly observed, possibly reflecting inaccuracies in construction of the densification maps.

At an applied pressure of 3 MPa, we expect that thermal cycling densification is dominated by power-law creep based on the densification map in Fig. 4(b). The experimental data at $P = 3$ MPa in Fig. 5(b) indeed appear to have a slope around $n = 4.3$, and compare very favorably to predictions of the power-law densification model [equation (4)], which are also shown in Fig. 5(b) for comparison. Finally, the predictions of equation (2) for diffusional densification shown in Fig. 5(b) fall significantly below the experimental data, further

emphasizing the enhancement of densification rates achievable by transformation-mismatch plasticity.

4.2. Final stage densification of unreinforced titanium powders

4.2.1. Final stage densification theory. Above relative densities of about 0.9, the geometry of compaction is described by the shrinkage of cavities isolated within a matrix, so the models for initial stage densification presented in the previous sections are no longer applicable. Arzt, Ashby *et al.* therefore model densification of an array of isolated spherical voids located at the corners of tetrakaidecahedral grains. For diffusive densification, Helle *et al.* [4] give the following simplified rate law:
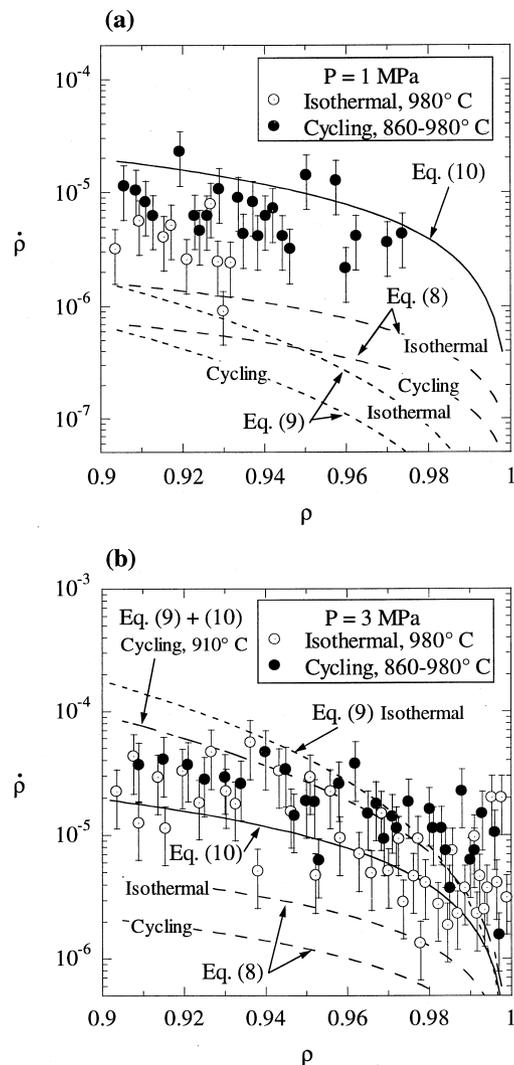

Fig. 6. Densification rates of unreinforced titanium as a function of relative density during the final stage of densification ($\rho > 0.90$) for applied pressures of (a) 1 MPa and (b) 3 MPa. The predictions of the final-stage densification models [equations (8)–(10)] are shown for comparison.

$$\dot{\rho} = 270 \cdot \frac{\Omega \cdot (1-\rho)^{1/2}}{k \cdot T \cdot r^3} \cdot \Bigg(\delta D_\text{b} + r$$

$$\cdot \left(\frac{1-\rho}{6} \right)^{1/3} \cdot D_\text{v} \Bigg) \cdot B_\text{f} \cdot P \qquad (8)$$

where the dimensionless constant B_f is introduced to account for a non-isostatic stress state, similar to the constant B_i used in equation (1) for initial stage densification. The numerical value of B_f is found to be about 1.8, as discussed in Appendix A.

The final stage densification rate due to power-law creep obeying equation (3) is given in Ref. [4] as:

$$\dot{\rho} = \frac{3}{2} \cdot C \cdot \frac{\rho \cdot (1-\rho)}{(1-(1-\rho)^{1/n})^n} \cdot \left(\frac{3}{2 \cdot n} \cdot B_\text{f} \cdot P \right)^n \quad (9)$$

With the transformation-mismatch plasticity constitutive law [equation (6)] in place of the creep law of equation (3), the densification rate is determined by analogy with equation (9) as:

$$\dot{\rho} = 3 \cdot \frac{\Delta V}{V} \cdot \frac{5 \cdot n'}{4 \cdot n' + 1} \cdot \frac{1}{\Delta t} \cdot (1-\rho) \cdot \frac{B_\text{f} \cdot P}{\sigma_\text{o}} \qquad (10)$$

4.2.2. Analysis of experimental data. Figures 6(a) and (b) show the measured densification rates of unreinforced titanium at 1 MPa and 3 MPa, respectively, for both isothermal and thermal cycling densification in the final stage. Thermal cycling produces a modest increase in densification rate at $P = 1$ MPa, but no clear enhancement is discernible at $P = 3$ MPa. For comparison with the data, the predictions of equations (8)–(10) are also shown in the figures.

The densification rates at $P = 1$ MPa [Fig. 6(a)] are accurately predicted within experimental error by equations (8) and (10) for isothermal and thermal cycling conditions, respectively. This result indicates that densification occurs by the diffusional mechanism during isothermal compaction, and by transformation-mismatch plasticity during thermal cycling. In contrast, the densification rates from power-law creep [equation (9)] are significantly lower than the measured rates for both isothermal and thermal cycling densification, and the diffusional mechanism [equation (8)] constitutes only a minor contribution to densification during thermal cycling. Since elimination of the final few percent of porosity is often the limiting step in densification processes, transformation-mismatch plasticity could present significant improvements in densification cycle times when low densification pressures are desired.

With applied stress of 3 MPa [Fig. 6(b)], the power-law mechanism plays a more dominant role in densification. For isothermal compaction, the densification rates predicted for this mechanism

[equation (9)] compare reasonably well with the experimental data, particularly at higher densities. During thermal cycling, both the power-law mechanism and the transformation-mismatch plasticity mechanism contribute significantly to densification. During each thermal cycle, transformation-mismatch plasticity occurs only at temperatures in the phase transformation range, while power-law densification occurs primarily at temperatures above this range, in the β-field. These mechanisms thus occur sequentially in time during each thermal cycle and can be considered independent, with the total average densification rate predicted by summing the rates of the two contributing mechanisms [equations (9) and (10)]. As shown in Fig. 6(b), the resulting prediction describes the thermal cycling densification data quite well over the full range of final stage densities. Finally, for both isothermal and thermal cycling densification, the rates predicted by the diffusional mechanism [equation (8)] are significantly slower than the measured rates.

4.3. Densification of composite powder blends

There is an abundance of experimental work which demonstrates that the constraining effect of rigid inclusions decreases the densification rate of powder blends, both for time-independent yield [36] and time-dependent mechanisms [10, 12]. The data collected during both isothermal and thermal cycling densification in the present work are in qualitative agreement with these observations (Fig. 3). In addition, many models have been published on the effect of rigid inclusions on densification [9, 11, 12, 14, 15], several of which are compatible with the densification models by Arzt, Ashby, and coworkers presented in the previous sections. In particular, the models of Bouvard [14] and Li and Funkenbusch [9, 11] contain similar mathematical treatments of the coordination of matrix and inclusion particles during densification. Bouvard [14] derived the following expression for the power-law densification rate of a composite (subscript c) in terms of the densification rate of the unreinforced matrix material (subscript m):

$$\left(\frac{\dot{\rho}}{\rho} \right)_\text{c} = \left(\frac{\dot{\rho}}{\rho} \right)_\text{m} \cdot \frac{1}{\Sigma^n} \qquad (11)$$

where Σ is a hardening parameter which increases with volume fraction of the inclusion phase, and which is predicted in closed form in a series of equations in Ref. [14]. A similar result was obtained by Besson and Evans [12] using a phenomenological densification law. These models are valid only for low volume fractions of reinforcement, below the percolation limit. A percolating structure of rigid particles can be expected to bear the majority of the applied load, dramatically reducing the densification

rate, or alternatively increasing the hardening parameter Σ.

Using equation (11), the hardening parameter Σ was calculated from the densification data of the composite powder blends. Because of the limited data acquired on composite powders at $P = 3$ MPa, only experiments conducted at $P = 1$ MPa are analyzed here. Furthermore, only initial stage densification is considered for simplicity. Since the initial-stage analytical models for both power-law creep and transformation-mismatch plasticity [equations (4) and (7)] have been found to represent the data for compaction of unreinforced titanium with reasonable accuracy, we use those equations to determine $(\dot{\rho}/\rho)_m$ in equation (11). The results of these calculations are shown in Fig. 7 for isothermal densification by power-law creep with $n = 4.3$. As expected, the hardening parameter is within experimental error equal to unity for the powder blend containing only 1 vol.% ZrO_2, which had a densification curve very similar to the unreinforced titanium [Fig. 3(a)]. Since the densification of the 5 vol.% and 10 vol.% blends only achieved densities around 0.75, the hardening parameter is only calculated over this small density interval. The hardening parameters for these composites are in the range $\Sigma = 1.5–2.5$.

Similar calculations of Σ were performed for the thermal cycling densification data, for which $n = 1$ is taken. The results are shown in Fig. 8, which is plotted in semi-logarithmic fashion to better display trends. Again the composite containing 1 vol.% ZrO_2 exhibits a hardening parameter near unity, but the other two composite systems have rapidly rising hardening parameters (i.e., rapidly dropping densification rates as compared to the unreinforced

material) which reach extremely large values as densification progresses.

Bouvard [14] furnishes a series of equations to predict the hardening parameter (which are too lengthy to present here) which show reasonable agreement with experimental studies of densification from the literature. The predictions of Bouvard's model are shown in Table 2 for 1, 5, and 10 vol.% rigid inclusions, along with the ranges of Σ determined from our experimental data (Figs 7 and 8). The agreement between the predictions and the model is very poor, particularly for the composites containing 5 and 10 vol.% ZrO_2, which exhibit much larger experimental values of Σ than expected. This discrepancy is discussed in terms of microstructural evolution in the following.

Figure 9 shows an optical micrograph of the composite powder blend containing 10 vol.% ZrO_2 densified by thermal cycling with applied stress $P = 1$ MPa. Within the titanium matrix surrounding the ZrO_2 particle, a lath- or colony-type microstructure is observed, revealing a significant zone of chemical reaction between the matrix and reinforcement. Such reaction was noted for other specimens containing 5 or 10 vol.% ZrO_2 subjected to both isothermal and thermal cycling densification. The pseudo-binary phase diagram of Ti–ZrO_2 [46] indicates that dissolution of ZrO_2 can be expected for all volume fractions of ZrO_2 investigated here, the result being the stabilization of α–Ti. The complete dissolution of 5 or 10 vol.% ZrO_2 in Ti would raise the α-transus to about 975°C or 1100°C, respectively.

We anticipate two major effects from the particle/matrix reaction, both of which can be expected to hinder densification, and therefore result in inflated values of Σ, as noted in
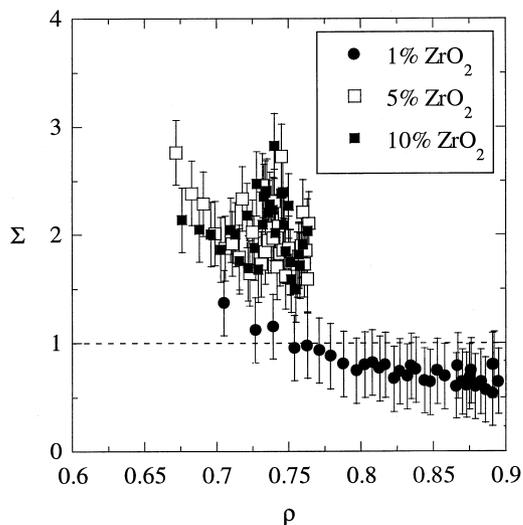

Fig. 7. Hardening parameter of composite powder blends as a function of relative density during isothermal densification at 980°C with applied uniaxial stress $P = 1$ MPa.
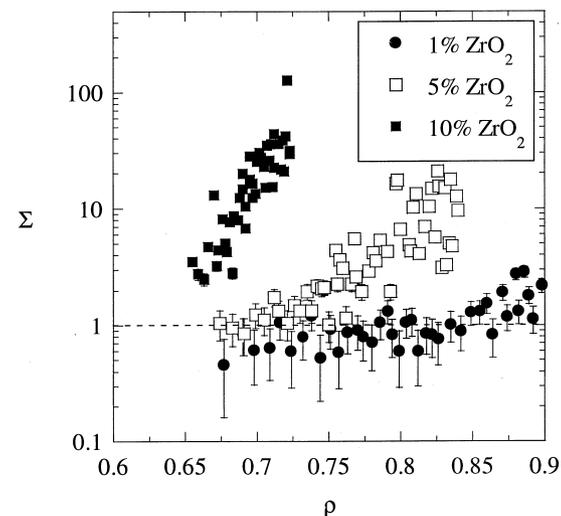

Fig. 8. Hardening parameter for thermally-cycled composite powder blends as a function of relative density with applied uniaxial stress $P = 1$ MPa.

Table 2. Hardening parameters [Σ from equation (8)] determined from the experimental data, compared with predictions of Bouvard [14] for both isothermal ($n = 4.3$) and thermal cycling densification ($n = 1$)

ZrO$_2$ content (vol.%)	$\Sigma(n = 4.3)$		$\Sigma(n = 1)$	
	Bouvard model	Experimental	Bouvard model	Experimental
1	1.03–1.11	0.65–1.3	1.02–1.07	0.5–3
5	1.08–1.17	1.5–3	1.10–1.14	1–20
10	1.15–1.25	1.5–3	1.20–1.24	2.5–42

Table 2. First, since the local dissolution of ZrO$_2$ stabilizes the α–Ti phase, and since α–Ti is much more creep resistant than β–Ti [39], the reaction will result in an effective increase in the volume fraction of non-densifying (or slowly-densifying) phase. This effect would be present for both isothermal and thermal cycling densification, and will result in only small effects in the early stages of reaction, amounting to an increase in the hardening parameter Σ. However, the percolation threshold for randomly packed spheres is typically between 0.16 and 0.26, depending on the size ratio of the matrix and reinforcement particles [47]. The development of a continuous network of non-densifying phase will result in a rapid reduction of densification rates. This may explain the dramatic increases in Σ observed for the 5 and 10 vol.% composite blends (Figs 7 and 8).

Second, since the dissolution of ZrO$_2$ shifts both the α- and β-transus of Ti to higher temperatures, the extent of the α/β phase transformation which drives transformation-mismatch plasticity will diminish as the reinforcement particles dissolve. This additional effect during thermal cycling provides a qualitative explanation for the difference in hardening parameters between the isothermally densified (Fig. 7) and thermally-cycled composite pow-
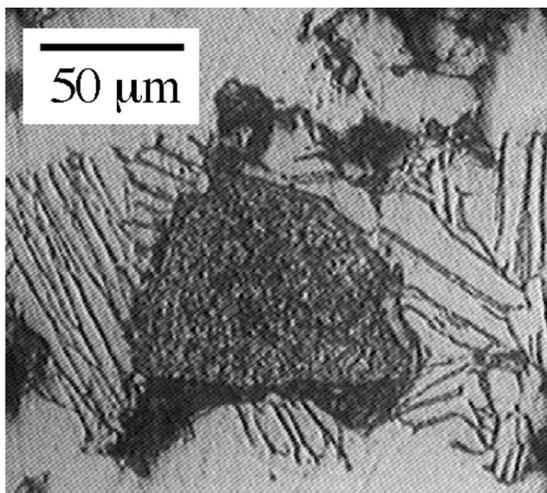

Fig. 9. Optical micrograph of a Ti/10 vol.% ZrO$_2$ composite powder blend densified by thermal cycling with $P = 1$ MPa, showing a zone of reaction between the reinforcement and matrix particles.

der blends (Fig. 8). Finally, although the Ti–ZrO$_2$ composite powders were not chemically inert, we note that the densification rates of the composites were generally increased by thermal cycling. If a more inert reinforcement (e.g., SiC fibers [48], TiC particulates or TiB whiskers [49]) were used instead of ZrO$_2$, thermal cycling could provide a rapid route for full composite densification.

5. CONCLUSIONS

The densification of titanium powders and Ti–ZrO$_2$ powder blends was investigated by uniaxial die pressing, both isothermally at 980°C and during thermal cycling between 860°C and 980°C (across the α/β phase transus of titanium). The following salient conclusions were drawn:

1. Thermal cycling through the phase transformation of titanium accelerates densification of unreinforced titanium and most of the ZrO$_2$-containing composite powder blends investigated. This enhancement is attributed to the emergence of transformation-mismatch plasticity as a densification mechanism, notably dominant at low applied pressures and/or higher densities. Densification mechanism maps have been constructed to compare isothermal and thermal-cycling densification.

2. The mechanistic densification models of Arzt, Ashby, *et al.* as summarized in Ref. [4], and the empirical densification model of Besson and Evans [12] are found to be mutually consistent for both the initial and final stages of densification. Comparison of these models allows the former theory to be adapted from the case of isostatic pressing to that of uniaxial die pressing.

3. When modified for the stress-state of uniaxial die-pressing, the densification models of Arzt, Ashby, *et al.* predict the experimental densification rates of pure titanium with reasonable accuracy during isothermal compaction. Adapting these models to the case of transformation-mismatch plasticity, we find excellent agreement between the thermal-cycling densification data and the model, both in the initial stage (relative density < 0.9) and in the final stage (relative density > 0.9) of densification.

4. Although thermal cycling increases the densification rate of composite powder blends containing

1, 5, or 10 vol.% ZrO_2 particles relative to isothermal compaction, the densification of the composites with 5 and 10 vol.% ZrO_2 was often much slower than for unreinforced titanium. This discrepancy was attributed to the dissolution of the reinforcement particles, and the attendant alteration of matrix chemistry, which strengthens the material and prevents phase transformation. It is anticipated that thermal-cycling densification could be used to rapidly produce composites if such reactions can be avoided by selection of an appropriate reinforcement.

REFERENCES

1. Wilkinson, D. S. and Ashby, M. F., *Acta metall.*, 1975, **23**, 1277.
2. Fischmeister, H. F. and Arzt, E., *Powder metall.*, 1983, **26**, 82.
3. Arzt, E., Ashby, M. F. and Easterling, K. E., *Metall. Trans.*, 1983, **14A**, 211.
4. Helle, A. S., Easterling, K. E. and Ashby, M. F., *Acta metall.*, 1985, **33**, 2163.
5. Lograsso, B. K. and Koss, D. A., *Metall. Trans.*, 1988, **19A**, 1767.
6. Choi, B. W., Deng, Y. G., McCullough, C., Paden, B. and Mehrabian, R., *Acta metall. mater.*, 1990, **38**, 2225.
7. Ashby, M. F., in *Powder Metallurgy: An Overview*, ed. I. Jenkins and J. V. Wood. The Institute of Metals, London, 1981, p. 144.
8. Duva, J. M. and Crow, P. D., *Acta metall. mater.*, 1992, **40**, 31.
9. Li, E. K. H. and Funkenbusch, P. D., *Metall. Trans.*, 1993, **24A**, 1345.
10. Taylor, N., Dunand, D. C. and Mortensen, A., *Acta metall. mater.*, 1993, **41**, 955.
11. Li, E. K. H. and Funkenbusch, P. D., *Acta metall.*, 1989, **37**, 1645.
12. Besson, J. and Evans, A. G., *Acta metall. mater.*, 1992, **40**, 2247.
13. Williamson, R. L., Knibloe, J. R. and Wright, R. N., *J. Eng. Mater. Technol.*, 1992, **114**, 105.
14. Bouvard, D., *Acta metall. mater.*, 1993, **41**, 1413.
15. Storakers, B., Fleck, N. A. and McMeeking, R. M., *J. Mech. Phys. Solids*, 1999, **47**, 785.
16. Pagounis, E., Talvitie, M. and Lindroos, V. K., *Mater. Res. Bull.*, 1996, **31**, 1277.
17. Wu, M. Y., Wadsworth, J. and Sherby, O. D., *Metall. Trans.*, 1987, **18A**, 451.
18. Greenwood, G. W. and Johnson, R. H., *Proc. Roy. Soc. Lond.*, 1965, **283A**, 403.
19. Wu, M. Y. and Sherby, O. D., *Scripta metall.*, 1984, **18**, 773.
20. Daehn, G. S. and Gonzalez-Doncel, G., *Metall. Trans.*, 1989, **20A**, 2355.
21. Pickard, S. M. and Derby, B., *Acta metall. mater.*, 1990, **38**, 2537.
22. Huang, C. Y. and Daehn, G. S., in *Superplasticity and Superplastic Forming 1995*, ed. A. K. Ghosh and T. R. Bieler. TMS, Warrendale PA, 1996, p. 135.
23. Dunand, D. C. and Myojin, S., *Mater. Sci. Eng.*, 1997, **230A**, 25.
24. Dunand, D. C. and Bedell, C. M., *Acta mater.*, 1996, **44**, 1063.
25. Schuh, C. and Dunand, D. C., *Scripta mater.*, 1999, **40**, 1305.
26. Kohara, S., *Metall. Trans.*, 1976, **7A**, 1239.
27. Oshida, Y., *J. Jap. Soc. Powder Metall.*, 1975, **22**, 147.
28. Ruano, O. A., Wadsworth, J. and Sherby, O. D., *Metall. Trans.*, 1982, **13A**, 355.
29. Leriche, D., Gautier, E. and Simon, A., in *International Conference on Powder Metallurgy ICPM '86*, 1986, pp. 1191–1195.
30. Leriche, D., Gautier, E. and Simon, A., in *Sixth World Conference on Titanium*, 1988, pp. 1295–1300.
31. Huang, C. Y. and Daehn, G. S., *Acta Mater*, 1996, **44**, 1035.
32. Schaefer, R. J. and Janowski, G. M., *Acta metall. mater.*, 1992, **40**, 1645.
33. Waldner, P., *Scripta mater.*, 1999, **40**, 969.
34. Stevens, R., in *Engineered Materials Handbook*, Vol. 4. ASM International, 1991, pp. 775–786.
35. Touloukian, Y. S., Kirby, R. K., Taylor, R. E. and Desai, P. D. (ed.), *Thermal Expansion: Metallic Elements and Alloys*. Plenum Press, New York, 1975.
36. Lange, F. F., Atteraas, L., Zok, F. and Porter, J. R., *Acta metall. mater.*, 1991, **39**, 209.
37. Wilkinson, D. S. and Ashby, M. F., in *4th International Conference on Sintering and Related Phenomena*, ed. G. C. Kuczynski. Plenum Press, New York, 1975, p. 473.
38. Arzt, E., *Acta metall.*, 1982, **30**, 1883.
39. Frost, H. J. and Ashby, M. F., *Deformation-Mechanism Maps: The Plasticity and Creep of Metals and Ceramics*. Pergamon Press, Oxford, 1982.
40. Schuh, C. and Dunand, D. C., *Acta mater.*, 1998, **46**, 5663.
41. Kot, R., Krause, G. and Weiss, V., in *The Science, Technology and Applications of Titanium*, ed. R. I. Jaffe and N. E. Promisel. Pergamon, Oxford, 1970, p. 597.
42. Schuh, C., Zimmer, W. and Dunand, D. C., in *Creep Behavior of Advanced Materials for the 21st Century*, ed. R. S. Mishra, A. K. Mukherjee and K. L. Murty. TMS, Warrendale PA, 1999, p. 61.
43. Zwigl, P. and Dunand, D. C., *Metall. Mater. Trans.*, 1998, **29A**, 2571.
44. Bouvard, D. and Ouedraogo, E., *Powder Tech.*, 1986, **46**, 255.
45. Piehler, H. R. and DeLo, D. P., *Prog. Mat. Sci.*, 1997, **42**, 263.
46. Domagala, R. F., Lyon, S. R. and Ruh, R., *J. Am. Ceram. Soc.*, 1973, **56**, 584.
47. Bouvard, D. and Lange, F. F., *Acta metall. mater.*, 1991, **39**, 3083.
48. Guo, Z. X. and Derby, B., *Acta metall. mater.*, 1994, **42**, 461.
49. Abkowitz, S., Weihrauch, P. F. and Abkowitz, S. M., *Ind. Heating*, 1993, **12**, 32.

APPENDIX A

Since the densification models of Arzt, Ashby, *et al.* [4] presented in the text have been derived for conditions of isostatic densification, it is necessary to consider the difference in stress state established by uniaxial die pressing. One approach, taken by Taylor *et al.* [10], consists of introducing two

dimensionless constants into the rate laws. In that work, the first constant was used in the same manner as B_i in the present paper. Taylor *et al.* considered densification to be controlled by the hydrostatic component of the applied stress state, and based on data of Bouvard and Ouedraogo [44], assigned $B_i = 2/3$. They introduced an additional constant based on the same data, which reduced the densification rate by an order of magnitude for the case of uniaxial die pressing.

The constant B_i, in its function assigned by Taylor *et al.* [10], attenuates the applied uniaxial pressure to describe the hydrostatic stress state during uniaxial die pressing. However, it has been noted that the deviatoric stress provides densification rate enhancement in experiments on aluminium and Ti–6Al–4V [45]. In an attempt to accurately predict densification under such conditions, Besson and Evans [12] derived the following rate equation for uniaxial die pressing where the deformation follows the power-law of equation (3):

$$\dot{\rho} = C \cdot \rho^2 \cdot \lambda^{n+1} \cdot P^n \qquad (A1)$$

in which λ is a density-dependent parameter determined by fitting experimental densification data with equation (A1). Besson and Evans determined λ for their experiments on Cu of different particle sizes, as well as for data of several other materials, and showed that all of the data sets could be fitted to equation (A1) with similar λ.

Alternatively, the power-law densification model used in the present work [equation (4)] is modified to describe uniaxial die pressing by the introduction of the dimensionless constant B_i. Combining equation (4) with equation (1) gives:

$$\dot{\rho} = 3.06 \cdot (\rho^2 \cdot \rho_o)^{1/3} \cdot \left(\frac{\rho - \rho_o}{1 - \rho_o}\right)^{1/2} \cdot C \cdot \left(\frac{B_i}{3}\right.$$
$$\left. \cdot \frac{P \cdot (1 - \rho_o)}{\rho^2 \cdot (\rho - \rho_o)}\right)^n \qquad (A2)$$

Since both equations (A1) and (A2) describe uniaxial die pressing with applied uniaxial stress P, they can be equated, yielding a relationship between λ and B_i:

$$\lambda = \left[3.06 \cdot \frac{\rho_o^{1/3}}{\rho^{4/3+2n}}\right.$$
$$\left. \cdot \left(\frac{\rho - \rho_o}{1 - \rho_o}\right)^{1/2-n} \cdot \left(\frac{B_i}{3}\right)^n\right]^{1/(n+1)} \qquad (A3)$$

During the final stage of densification, assuming that power-law creep is still the dominant densification mechanism, equation (A2) is replaced by equation (9), yielding the following relationship between λ and B_f:

$$\lambda = \left[\frac{3}{2} \cdot \frac{1 - \rho}{\rho \cdot (1 - (1 - \rho)^{1/n})^n}\right.$$
$$\left. \cdot \left(\frac{3}{2 \cdot n} \cdot B_f\right)^n\right]^{1/(n+1)} \qquad (A4)$$

The function λ has been noted to vary slightly between different materials and even between powders of the same material with different particle sizes [12]. In the present work we are concerned with densification of Ti powders of mean particle diameter 80–100 μm. Therefore, we take data of Besson and Evans [12] for Cu with particle diameters between 50 and 100 μm as the best match to our conditions. The density-dependence of this value of λ is shown in Fig. A1. With a creep stress exponent $n = 2$ measured by Besson and Evans [12] on dense specimens of copper, equation (A3) is best-fitted to the initial stage densification data ($\rho < 0.9$) with $B_i = 1.1$. Similarly, equation (A4) is best-fitted to the final stage densification data ($\rho > 0.9$) with $B_f = 1.8$. Equations (A3) and (A4) are plotted in Fig. A1 for comparison with the data of Besson and Evans.

The very good agreement between the experimental values of λ and equations (A3) and (A4) shows that the empirical modeling approach of Besson and Evans and the mechanistic, analytical approach of Arzt, Ashby, and coworkers are compatible. This comparison also suggests that the Arzt, Ashby, *et al.* models of densification presented in the text can be adapted to uniaxial die pressing with the introduction of $B_i = 1.1$ in equation (1) and $B_f = 1.8$ in equations (8)–(10). However, we note again that λ is somewhat sensitive to changes in powder particle
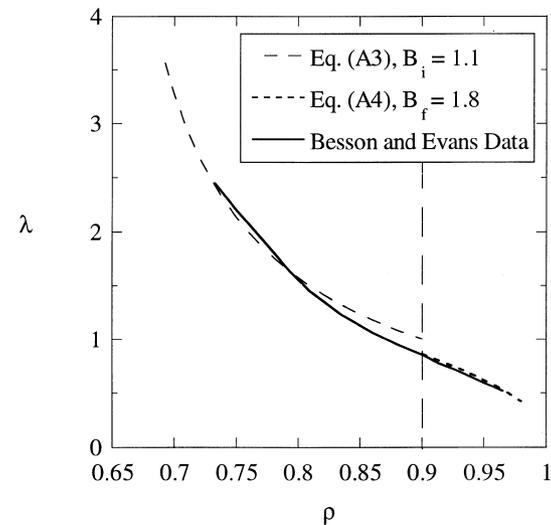

Fig. A1. Comparison of densification parameter λ determined experimentally by Besson and Evans [12] and predicted by equation (A3) using $B_i = 1.1$ and by equation (A4) using $B_f = 1.8$.

size [12], so different values of B_i or B_f may be appropriate under other circumstances. Finally, the value of $B_i = 1.1$ predicts about a factor of two increase in the average interparticle contact pressure compared to that predicted by Taylor *et al.* [10] ($B_i = 2/3$) which considered only the global hydrostatic stress, neglecting the deviatoric component. Indeed, experiments on aluminium and Ti–6Al–4V [45] demonstrate a densification rate enhancement due to the presence of a deviatoric uniaxial stress. Since $B_f = 1.8$ is greater than $B_i = 1.1$, the effect of deviatoric stresses is greater during final stage densification as compared to the initial stage.

APPENDIX B

Nomenclature

$\dot{\varepsilon}$	strain rate during isothermal creep (/s)
$\bar{\dot{\varepsilon}}$	mean strain rate during thermal cycling (/s)
λ	density-dependent parameter to describe densification for uniaxial die pressing
ρ	relative density
ρ_o	initial relative density of packed powder
$\dot{\rho}$	densification rate (/s)
σ	applied uniaxial stress for creep (MPa)
σ_t	transition stress between dislocation creep and power-law breakdown (MPa)
σ_o	spatial and time-averaged internal stress during allotropic phase transformation (MPa)
Ω	atomic volume (m^3)
B_i, B_f	geometry-dependent constants for densification in the initial (i) and final (f) stages
C	creep constant (MPa^{-n}/s)
δD_b	grain-boundary diffusivity (m^2/s)
D_v	volume diffusivity (m^3/s)
G	temperature-dependent shear modulus (GPa)
n	stress exponent for creep
n'	stress exponent for creep of the weaker allotropic phase during transformation-mismatch plasticity
P	externally applied pressure (MPa)
P_{eff}	interparticle contact pressure (MPa)
r	average powder particle radius (m)
Δt	period of thermal cycles (s)
$\Delta V/V$	volume change during allotropic phase transformation